

Trispectrum reconstruction of non-Gaussian noise

Guy Ramon*

Department of Physics, Santa Clara University, Santa Clara, CA 95053

Using a qubit to probe non-Gaussian noise environments is theoretically studied in the context of classical random telegraph processes. Protocols for control pulses are developed to effectively scan higher noise correlations, offering valuable information on the charge environment of the qubit. Specifically, the noise power spectrum and trispectrum are reconstructed simultaneously for a wide range of qubit-fluctuator coupling strengths, demonstrating the method's robustness. These protocols are readily testable in various qubit systems with well-developed quantum control, including quantum dot spins, superconducting qubits and NV centers in diamond.

Introduction. The decoherence experienced by all solid-state qubits is largely determined by their immediate environment that typically includes fluctuating charges and spins of nuclei or local electron. While unavoidable interactions with the environment continue to limit the number of qubits that can be coherently manipulated and entangled, recent studies attempt to harness qubit susceptibility to local fluctuations by transforming them into high-resolution sensitive probes of their environment. Valuable on its own [1], noise spectroscopy is anticipated to help mitigating decoherence more effectively, by, e.g., modifying the physical hosting system or adjusting the qubit control schemes.

In recent years a growing body of works across a wide range of quantum systems has been devoted to exploring strategies to characterize environmental noise by measuring the dynamics of properly initialized and controlled qubits [2]. Operating a qubit under a sequence of dynamical decoupling (DD) pulses was shown to establish a simple relation between the measured qubit signals and the noise power spectrum [3–6]. Dynamically decoupling a qubit afflicted by Gaussian phase noise effectively generates a frequency-domain filter determined by the pulse sequence [7]. For periodic sequences with a fixed pulse interval τ , the filter is sharply peaked at a frequency $f = 1/2\tau$ and its odd harmonics, allowing one to scan the noise spectrum by subjecting the qubit to sequences with varying pulse intervals. This method of DD-based noise spectroscopy (DDNS) has been used to reconstruct environmental noise in various qubit platforms, including trapped ions [8, 9], superconducting circuits [4, 10], semiconductor quantum dots (QDs) [11–13], phosphorous donors in silicon [14], and NV centers in diamond [15–17].

DDNS has been limited by several approximations in the underlying theory and method implementation, namely, the qubit is assumed to undergo pure dephasing by coupling longitudinally to the noise, and the noise is taken to be both classical and Gaussian. Several recent theoretical studies have put forth qubit control protocols that allow, in principle, to extend the applicability of DDNS methods to non-Gaussian [18], and quantum [19, 20] noise environments.

Focusing on the assumption of noise Gaussianity, we note that a Gaussian process is most often the result of a collection of many uncorrelated (or weakly correlated) processes, e.g., when the qubit interacts with a large environment, so that all higher correlation functions factorize into products of one-

and two-point correlators. This picture breaks down when high-resolution sensing of small environments strongly coupled to the qubit is pursued, or when environmental dynamics with strong and nontrivial spatial correlations is present due to interactions between its constituents [21, 22]. Furthermore, solid-state devices are commonly afflicted with low-energy excitations, such as slowly switching two-level fluctuators (TLFs) that are responsible for $1/f$ noise [23, 24], which is inherently non-Gaussian, thus in many realistic scenarios a complete noise characterization must include higher correlations and their respective noise cumulants.

In this letter we study reconstruction of polyspectra — the Fourier transforms of multi-point correlators — of a classical Random Telegraph Noise (RTN) process, building on an approach proposed by Norris *et al.* [18]. Using carefully chosen sequences of DD pulses, we adapt the method to reconstruct the RTN power spectrum and trispectrum. The central role of charge noise in limiting qubit coherence has been long established in various platforms such as Josephson qubits [25, 26], and QDs [27, 28], and was more recently reaffirmed in both [29] Si/SiGe [13, 30, 31], and GaAs [32, 33] QD spin qubits. Moreover, RTN sources are the quintessential testbed for non-Gaussian noise spectroscopy protocols, owing in part to the ability to control the non-Gaussianity probed by the qubit by tuning the coupling strength to switching rate ratio, η . As η increases, pronounced non-Gaussian behavior is formed, exhibiting, e.g., plateaus in the qubit decay signal [34, 35]. We provide explicit control protocols that are readily accessible in various solid-state qubit systems, explain the numerical challenges associated with polyspectra reconstruction, and offer their resolution.

Before discussing our results, we mention that other approaches to quantify non-Gaussian noise have been considered, including approximate resummation of the cumulant series [36], appropriate for the special case of quadratic coupling to a Gaussian noise (e.g., at an optimal working point), and a non-perturbative spectroscopy method that was demonstrated for non-Gaussian discrete magnetic noise, strongly coupled to the qubit [37].

Formalism. At pure dephasing, the qubit-TLF Hamiltonian reads $\mathcal{H} = b_z(t)\hat{\sigma}_z/2$, where $b_z(t) = v\xi(t)$, v is the coupling strength, $\xi(t) = \pm 1$ represents the RTN stochastic variable switching between the two states with an average rate γ , and we assume for simplicity that the average times spent at each

state are equal (i.e., symmetric TLF). Qubit dephasing at read-out time T is manifested in the off-diagonal elements of its density matrix, $\hat{\rho}_Q(T)$, which is constructed from the evolution operator including any control pulses. Qubit coherence is then quantified by:

$$W(T) \equiv \frac{\langle + | \hat{\rho}_Q(T) | - \rangle}{\langle + | \hat{\rho}_Q(0) | - \rangle} = \left\langle e^{-i\phi(T)} \right\rangle \equiv e^{-\chi(T)}, \quad (1)$$

where $\langle \cdot \rangle$ denotes averaging over realizations of the classical RTN (or partial trace of the environmental degrees of freedom for quantum noise). For any noise, a formal solution to the attenuation factor, $\chi(T)$, can be written in terms of a cumulant expansion [7, 38]

$$\chi(T) = - \sum_{k=1}^{\infty} \frac{(-iv)^k}{k!} C_k(T), \quad (2)$$

where the k th cumulant of the noise, $C_k(T)$, includes all connected diagrams of that order and can be written in terms of the noise moments. We assume qubit evolution under a sequence of n_p ideal π pulses about the x or y axes defined by the switching function: $f_T(t) = \sum_{j=0}^{n_p} (-1)^k \Theta(t - t_j) \Theta(t_{j+1} - t)$, where we take $t_0 = 0$ and $t_{n_p+1} = T$. For a given switching function, the k th cumulant is found as

$$C_k(T) = \int_0^T f_T(t_1) dt_1 \cdots \int_0^T f_T(t_k) dt_k A_k(t_1, \dots, t_k), \quad (3)$$

where $A_k(t_1, \dots, t_k)$ includes all the j -point correlation functions, $\langle \xi(t_1) \cdots \xi(t_j) \rangle$, up to $j = k$. For stationary noise, the correlators depend only on time separations, $\tau_j \equiv t_{j+1} - t_1$, $j \in 1, \dots, k-1$, and the cumulants can be evaluated in Fourier space:

$$C_k(T) = \int_{\mathbb{R}^{k-1}} \frac{d\vec{\omega}_{k-1}}{(2\pi)^{k-1}} \prod_{j=1}^{k-1} \tilde{f}_T(\omega_j) \tilde{f}_T(-\Sigma \vec{\omega}_{k-1}) S_{k-1}(\vec{\omega}_{k-1}), \quad (4)$$

where $\tilde{f}_T(\omega)$ is the Fourier transform of the switching function, known as the filter function, $\vec{\omega}_k \equiv (\omega_1, \dots, \omega_k)$, $\Sigma \vec{\omega}_k \equiv \omega_1 + \dots + \omega_k$, and we introduced the polyspectra [18]:

$$S_k(\vec{\omega}_k) = \int_{\mathbb{R}^k} d\vec{\tau}_k e^{-i(\vec{\omega}_k \cdot \vec{\tau}_k)} A_{k+1}(\vec{\tau}_k). \quad (5)$$

For Gaussian noise all higher noise moments factorize to products of lower moments and their respective cumulants vanish. Furthermore, if the Gaussian noise has zero mean, $\langle \xi(t) \rangle = 0$, it is fully characterized by its two-point correlation function, or equivalently by its Fourier transform—the power spectral density (PSD), also referred to as the first spectrum [39]. In contrast, a complete account of a non-Gaussian noise must include all cumulants and their respective polyspectra.

We now apply this formalism to treat the case of a single RTN. The noise generated by a symmetric TLF has zero mean and all odd noise moments and cumulants vanish, thus

the resulting attenuation factor given by Eq. 2 includes only decay with no phase contribution. Starting from the two- and four-point correlators: $\langle \xi(t_1) \xi(t_2) \rangle = e^{-2\gamma|t_1-t_2|}$, and $\langle \xi(t_1) \xi(t_2) \xi(t_3) \xi(t_4) \rangle = e^{-2\gamma(t_4-t_3+t_2-t_1)}$, $t_1 \leq t_2 \leq t_3 \leq t_4$, with corresponding permutations for other time orderings [7, 40], we have $A_2(t_1, t_2) = \langle \xi(t_1) \xi(t_2) \rangle$, and

$$A_4(t_1, t_2, t_3, t_4) = \langle \xi(t_1) \xi(t_2) \xi(t_3) \xi(t_4) \rangle - A_2(t_1, t_2) \times A_2(t_3, t_4) - A_2(t_1, t_3) A_2(t_2, t_4) - A_2(t_1, t_4) A_2(t_2, t_3).$$

The resulting PSD and trispectrum are found respectively as

$$S_1(\omega) = \frac{4\gamma}{4\gamma^2 + \omega^2}, \quad (6)$$

and [41] (see section I of the supplemental material [42])

$$S_3(\vec{\omega}_3) = -16\gamma \frac{48\gamma^4 + 4\gamma^2 \sum_{i \leq j} \omega_i \omega_j + \omega_1 \omega_2 \omega_3 \Sigma \vec{\omega}_3}{\prod_{i=1}^3 (4\gamma^2 + \omega_i^2) (4\gamma^2 + (\Sigma \vec{\omega}_3)^2)}. \quad (7)$$

For free induction decay (FID) or simple pulse sequences, such as periodic dynamical decoupling (PDD) and Carr-Purcell-Meiboom-Gill (CPMG), the second and fourth cumulants of a single classical RTN were calculated analytically in time domain using Eq. (3) [7, 35], matching the results obtained from Eq. (4) by direct integration of Eqs. (6) and (7). Polyspectra of any classical noise are highly symmetric and are fully specified by their values within a frequency space known as the principal domain [18, 43]. Whereas the PSD possesses a single (even) symmetry that defines its principal domain as all non-negative frequencies, the trispectrum is invariant under 48 operations, as detailed in section II of the supplemental material.

DDNS protocols rely on the application of pulse sequences whose filter functions are characterized by a fundamental frequency, $2\pi/T$, and its harmonics, effectively acting as frequency combs [3]. Recently scrutinized [44], the accuracy of this so-called delta approximation improves significantly by repetition of the base sequences, effectively extending the measurement time to MT , where M is the number of repetitions [45]. Extending these protocols to non-Gaussian noise spectroscopy relies on the ability of pulse sequences to form multidimensional frequency combs necessary for polyspectra reconstruction [18]. Approximating the filter functions with multidimensional dirac combs allows us to replace the frequency integrals in Eq. (4) with summations, truncated at frequencies where either the filter function or the polyspectrum (or both) are sufficiently small. The resulting approximate second and fourth cumulants are:

$$C_2(MT) \approx \frac{M}{T} \sum_{n \in \mathcal{D}_1} \Omega_1(n) \left| \tilde{f}_T\left(\frac{2\pi n}{T}\right) \right|^2 S_1\left(\frac{2\pi n}{T}\right) \quad (8)$$

$$C_4(MT) \approx \frac{M}{T^3} \sum_{\vec{n}_3 \in \mathcal{D}_3} \Omega_3(\vec{n}_3) \prod_{j=1}^3 \tilde{f}_T\left(\frac{2\pi \vec{n}_3(j)}{T}\right) \times \tilde{f}_T\left(-\frac{2\pi \Sigma \vec{n}_3}{T}\right) S_3\left(\frac{2\pi \vec{n}_3}{T}\right), \quad (9)$$

where $\mathcal{D}_1 = \{0, 1, \dots, n^{\max}\}$ denotes the discretized principal domain of the PSD, truncated at frequency $2\pi n^{\max}/T$, and the corresponding multiplicity is $\Omega_1(n) = 2 - \delta_{n,0}$. Likewise, \vec{n}_3 denotes all three-tuple integers up to n_3^{\max} within the trispectrum discretized and truncated principal domain, \mathcal{D}_3 , with corresponding multiplicity, Ω_3 [42].

The final step needed in order to form a finite set of equations connecting the polyspectra to measurable qubit signals, is to truncate the cumulant series in Eq. (2), thereby treating non-Gaussian terms perturbatively. In the context of RTN spectroscopy this approximation seems to suggest that we are limited to weak coupling, $\eta = v/\gamma \ll 1$. Nevertheless, the noise reconstruction procedure described below can be used to extract valuable information on the charge environment even when it is strongly coupled to the qubit.

DDNS Protocols. The original DDNS protocol proposed by Álvarez and Suter [3] utilized a set of 2-pulse CPMG sequences with variable sequence times: $T_i = T, T/2, \dots, T/n^{\max}$, scanning the spectrum with a resolution of $\omega_{\min} = 2\pi/T$ up to spectral bound of $\omega_{\max} = 2\pi n^{\max}/T$. Non-Gaussian DDNS requires a large number of distinct sequences to support the reconstruction of multidimensional grids of frequency points. Following Norris *et al.*, we construct a pool of base sequences comprising Mixed-order Concatenated DD (MCDD) segments with orders between 0 to 5. FID segments are included to avoid full refocusing of static noise, which is important for polyspectra reconstruction as the number of points with zero frequency becomes substantial. All base sequences have a fixed time $T = 256\delta = 16/\gamma$, where δ is the time resolution providing a theoretical upper bound of π/δ for the frequency cutoff, and time is scaled with inverse RTN switching rate, γ [46]. Other requirements imposed on the MCDD sequences included in the pool are detailed in the section III of the supplemental material. Setting harmonics bounds at $n^{\max} = 32$, and $n_3^{\max} = 8$, the reconstructed PSD and trispectrum are truncated at frequencies $\pi/4\delta$, and $\pi/16\delta$, respectively. Retaining only the second and fourth cumulants, the set of linear equations that is formed by inserting Eqs. (8) and (9) into Eq. (2) can be cast as

$$\vec{\chi} = A \begin{pmatrix} \vec{S}_1 \\ \vec{S}_3 \end{pmatrix}. \quad (10)$$

Our aforementioned harmonics bounds correspond to $n_{\text{PSD}} = 33$ and $n_{\text{TRI}} = 285$ frequency points in the PSD and trispectrum, respectively, thus $n_{\text{seq}} = 318$ sequences and corresponding signal measurements are needed. The reconstruction matrix, A , connects these measured signals with the PSD and trispectrum. We stress that restricting the reconstruction to frequencies within the principal domains is not only advantageous in reducing the number of equations to be solved — it is, in fact, essential in order to avoid singularities in A .

Reconstruction Results. Several factors limit our ability to reconstruct non-Gaussian noise by introducing errors into Eq. (10): (i) truncation of the cumulant expansion, (ii) inaccuracy of the delta approximation in the spectroscopic formulas, Eqs. (8) and (9), (iii) frequency cutoffs in the truncated

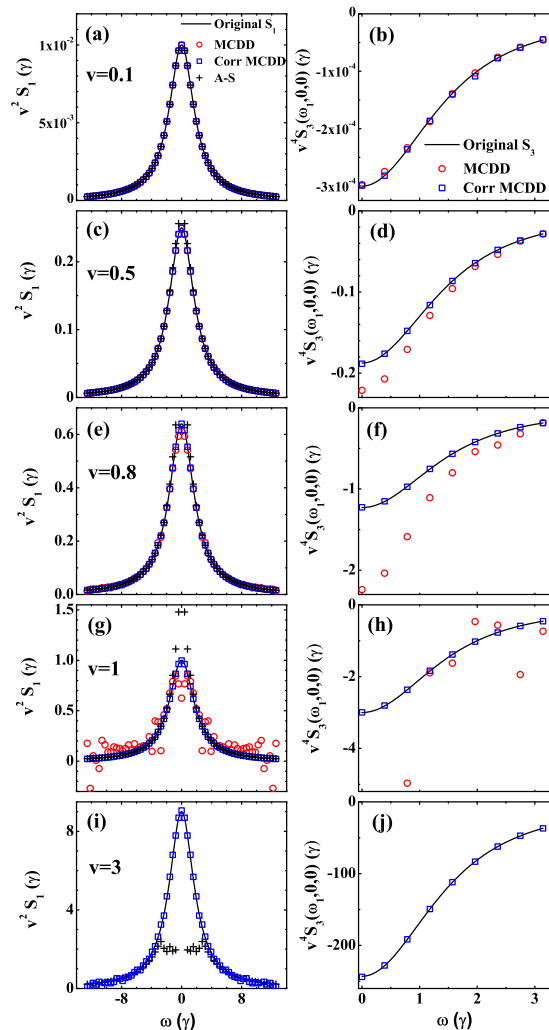


FIG. 1. (Color online) RTN reconstruction of PSD (panels a, c, e, g, i) and trispectrum cut, $\omega_2 = \omega_3 = 0$ (panels b, d, f, h, j). Starting at top row, coupling strengths are $v = 0.1, 0.5, 0.8, 1$, and 3 . Solid lines correspond to the theoretical spectra, Eqs. (6) and (7), red circles depict reconstructions with sets of MCDD sequences, optimized for each v , and blue squares show corrected results based on a-priori knowledge of the RTN parameters (see main text). At $v = 3$ (panels (i) and (j)), uncorrected polyspectra reconstruction with only the first two cumulants is no longer practical. Black pluses in the PSD panels depict Gaussian reconstruction with the Álvarez-Suter protocol, which is inadequate at strong coupling (see panel (i)). Frequencies are measured in units of RTN switching rate, γ .

principal domains, and (iv) numerical errors in the matrix inversion due to large condition numbers. Whereas the first error predominantly depends on the noise non-Gaussianity, dictated by the RTN parameters, the other three errors can be substantially reduced by appropriate selection of control sequences. Crucially, however, sequences that minimize errors due to discretization and frequency truncation tend to provide similar spectral filtering, resulting in numerical instabilities. Moreover, at weak coupling, where contributions from the neglected higher cumulants are insignificant, trispectrum reconstruction is nevertheless challenging as it requires very strin-

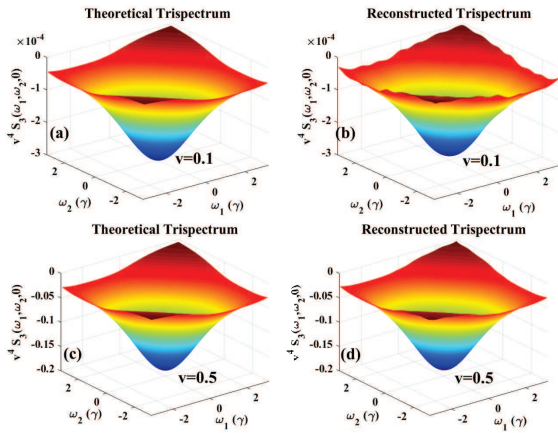


FIG. 2. (Color online) Theoretical and reconstructed RTN trispectrum cuts at $\omega_3 = 0$ for two coupling strengths. Spline interpolation was used to smoothen the reconstructed values in plots (b) and (d). The same sequence set, optimized for $v = 0.1$ was used for both reconstructions.

gent error thresholds on the second cumulant, since its related matrix elements are much larger than those associated with the fourth cumulant.

We have developed a layered algorithm for optimized selection of sets of control sequences that balances between these conflicting requirements, enabling us to obtain faithful reconstructions of the PSD and trispectrum of single RTNs over a wide parameter range. Our sequence selection is primarily based on maximizing the accuracy of the cumulants evaluation, given predefined finite sets of frequency points in \mathcal{D}_1 and \mathcal{D}_3 . Minimizing both absolute (for each sequence) and relative (within the entire sequence set) errors, as well as ensuring low condition numbers for the reconstruction matrix, A , are all crucial for successful reconstruction, as detailed in section III of the supplemental material. The resulting set of control sequences are recorded in A , and their corresponding qubit attenuation factors, $\chi(T)$, are calculated exactly for a given RTN, using a transfer matrix method [35, 47]. Fig. 1 demonstrates PSD and trispectrum reconstructions for RTN with several coupling strengths. Polyspectra of order n are plotted with a prefactor of v^{n+1} , to represent their weighted contribution in the reconstruction matrix.

As coupling strength increases, non-Gaussianity becomes more pronounced and errors due to the cumulant series truncation dominate. We disentangle this (physical) error from the other (numerical) errors by applying a correction term to the attenuation factors used in Eq. (10) that accounts for the truncated cumulants. The resulting corrected reconstructions are depicted by blue squares in Fig. 1 and their excellent agreement with the theoretical spectra shows that all other errors have been successfully minimized through our sequence selection procedure. We stress that while the cumulant correction term requires a-priori knowledge of the RTN parameters and is thus not directly applicable for experimentally measured qubit signals afflicted by an unknown noise source, our

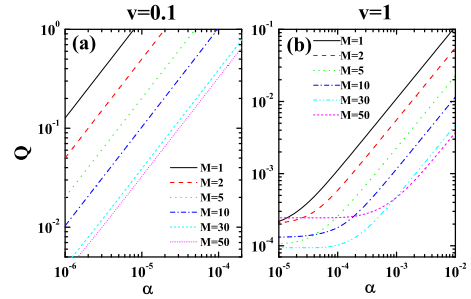


FIG. 3. (Color online) Trispectrum reconstruction quality, \mathcal{Q} , vs. relative measurement noise amplitude, α , with several base sequence repetitions for RTN coupling strengths of: (a) $v = 0.1$; (b) $v = 1$. Sequence sets are optimized for each M and v value. In panel (b) reconstructions are corrected to account for truncated polyspectra higher than S_3 .

preliminary work suggests that with a reasonable overhead one can employ a feedback loop to simultaneously optimize noise reconstruction and identify the unknown RTN parameters. Since the set of control sequences optimized for weak coupling reconstruction satisfies the more stringent second cumulant error requirements, we expect and observe that the same protocol provides adequate reconstruction at stronger couplings, as long as cumulant error correction is applied for $v \gtrsim 0.5$. This is demonstrated in Fig. 2, where, unlike the results shown in Fig. 1, we use a single set optimized for $v = 0.1$, for trispectra reconstruction at larger coupling strengths (see section III of the supplemental material for additional details).

We studied the robustness of our noise reconstruction against measurement errors and the number of base sequence repetitions, M [48]. In Fig. 3 we plot the reconstruction quality \mathcal{Q} , defined as

$$\mathcal{Q} \equiv \frac{1}{n_{\text{TRI}}} \sum_{\vec{n}_3 \in \mathcal{D}_3} \left| \frac{S_3 \left(\frac{2\pi\vec{n}_3}{T} \right) - S_3^{\text{rec}} \left(\frac{2\pi\vec{n}_3}{T} \right)}{S_3 \left(\frac{2\pi\vec{n}_3}{T} \right)} \right|, \quad (11)$$

against the measurement noise amplitude, α , relative to the qubit signal, for several M values and two coupling strengths (see section IV of the supplemental material for more details on our measurement error simulations and protocol robustness). Here, we have employed sequence sets optimized for each given M and v . At weak coupling, the dominant factor limiting reconstruction quality is cumulant errors due to the delta approximation. With increased M , this approximation becomes more accurate, resulting in consistent improvement in \mathcal{Q} . Interestingly, at larger coupling strengths, after applying the cumulant correction term, the reconstruction quality is limited by condition number instabilities, which tend to be stronger at larger M , where the filter function peaks are narrower. As shown in Fig. 3(b), increasing M in this case is not always beneficial, even in the idealized scenario of perfect π -pulses shown here. Using a pulse sequence set optimized for given v and M to reconstruct polyspectra of RTN under different conditions always results in larger cumulant errors and consequently poorer reconstruction.

Conclusions We developed control sequence protocols for trispectrum reconstruction of RTN sources. These protocols are shown to be robust over a wide range of RTN parameters, and can be used to identify and characterize single RTN sources in a variety of qubit platforms. We plan to extend this work in subsequent studies by developing control protocols that will map two and more RTN sources, and treat quantum TLFs in the strong coupling regime [49, 50]. Non-Gaussian noise spectroscopy can also be used to shed light on the role of TLF interactions in generating $1/f$ noise [22, 51, 52]. The current work can be viewed as complementary to a very recent experimental demonstration of non-Gaussian noise spectroscopy that utilized a flux superconducting qubit as a probe [10]. Whereas the non-Gaussian signatures there were observed in the phase evolution of the qubit's coherence, captured to leading order by the bispectrum, the non-Gaussianity of our RTN process is encoded to leading order in the trispectrum, as part of the signal decay. The multilayered sequence selection algorithm that we utilize to resolve numerical instabilities inherent in the original proposal [18] also differs from the maximum likelihood approach taken in [10].

Acknowledgements The author wishes to thank Łukasz Cywiński for useful discussions. This work was supported by the National Science Foundation Grant no. DMR 1829430.

* gramon@scu.edu

- [1] C. L. Degen, F. Reinhard, and P. Cappellaro, *Rev. Mod. Phys.* **89**, 035002 (2017).
- [2] P. Szańkowski, G. Ramon, J. Krzywda, D. Kwiatkowski and Ł. Cywiński, *J. Phys.: Condens. Matter* **29**, 333001 (2017).
- [3] Gonzalo A. Álvarez and Dieter Suter, *Phys. Rev. Lett.* **107**, 230501 (2011).
- [4] Jonas Bylander, Simon Gustavsson, Fei Yan, Fumiki Yoshihara, Khalil Harrabi, George Fitch, David G. Cory, Yasunobu Nakamura, Jaw-Shen Tsai and William D. Oliver, *Nature Phys.* **7**, 565 (2011).
- [5] Ido Almog, Yoav Sagi, Goren Gordon, Guy Bensky, Gershon Kurizki and Nir Davidson, *J. Phys. B* **44**, 15400 (2011).
- [6] Tatsuro Yuge, Susumu Sasaki, and Yoshiro Hirayama, *Phys. Rev. Lett.* **107**, 170504 (2011).
- [7] Ł. Cywiński, Roman M. Lutchyn, Cody P. Nave and S. Das Sarma, *Phys. Rev. B* **77**, 174509 (2008).
- [8] Michael J. Biercuk, Hermann Uys, Aaron P. VanDevender, Nobuyasu Shiga, Wayne M. Itano and John J. Bollinger, *Nature* **458**, 996 (2009).
- [9] Shlomi Kotler, Nitzan Akerman, Yinnon Glickman, Anna Kesselman and Roe Ozeri, *Nature* **473**, 61 (2011).
- [10] Yungkyu Sung, Félix Beaudoin, Leigh M. Norris, Fei Yan, David K. Kim, Jack Y. Qiu, Uwe von Lüepke, Jonilyn L. Yoder, Terry P. Orlando, Lorenza Viola, Simon Gustavsson, and William D. Oliver, arXiv:1903.01043 (unpublished).
- [11] J. Medford, Ł. Cywiński, C. Barthel, C. M. Marcus, M. P. Hanson, and A. C. Gossard, *Phys. Rev. Lett.* **108**, 086802 (2012).
- [12] K. W. Chan, W. Huang, C. H. Yang, J. C. C. Hwang, B. Hensen, T. Tanttu, F. E. Hudson, K. M. Itoh, A. Laucht, A. Morello, and A. S. Dzurak, *Phys. Rev. Appl.* **10**, 044017 (2018).
- [13] Erika Kawakami, Thibaut Jullien, Pasquale Scarlino, Daniel R. Ward, Donald E. Savage, Max G. Lagally, Viatcheslav V. Dobrovitski, Mark Friesen, Susan N. Coppersmith, Mark A. Eriksson, and Lieven M. K. Vandersypen, *PNAS* **113**, 11738 (2016).
- [14] Juha T. Muhonen, Juan P. Dehollain, Arne Laucht, Fay E. Hudson, Rachpon Kalra, Takeharu Sekiguchi, Kohei M. Itoh, David N. Jamieson, Jeffrey C. McCallum, Andrew S. Dzurak and Andrea Morello, *Nature Nanotech.* **9**, 986 (2014).
- [15] N. Bar-Gill, L. M. Pham, C. Belthangady, D. Le Sage, P. Cappellaro, J. R. Maze, M. D. Lukin, A. Yacoby and R. Walsworth, *Nature Comm.* **3**, 858 (2012).
- [16] T. Staudacher, F. Shi, S. Pezzagna, J. Meijer, J. Du, C. A. Meriles, F. Reinhard, J. Wrachtrup, *Science* **339**, 561 (2013).
- [17] Y. Romach, C. Müller, T. Unden, L. J. Rogers, T. Isoda, K. M. Itoh, M. Markham, A. Stacey, J. Meijer, S. Pezzagna, B. Naydenov, L. P. McGuinness, N. Bar-Gill, and F. Jelezko, *Phys. Rev. Lett.* **114**, 017601 (2015).
- [18] Leigh M. Norris, Gerardo A. Paz-Silva, and Lorenza Viola, *Phys. Rev. Lett.* **116**, 150503 (2016).
- [19] Gerardo A. Paz-Silva, Seung-Woo Lee, Todd J. Green and Lorenza Viola, *New J. Phys.* **18**, 073020 (2016).
- [20] Gerardo A. Paz-Silva, Leigh M. Norris, and Lorenza Viola, *Phys. Rev. A* **95**, 022121 (2017).
- [21] A. A. Clerk, M. H. Devoret, S. M. Girvin, Florian Marquardt, and R. J. Schoelkopf, *Rev. Mod. Phys.* **82**, 1155 (2010).
- [22] Jürgen Lisenfeld, Grigorij J. Grabovskij, Clemens Miller, Jared H. Cole, Georg Weiss and Alexey V. Ustinov, *Nature Comm.* **6**, 6182 (2015).
- [23] E. Paladino, L. Faoro, G. Falci, and Rosario Fazio, *Phys. Rev. Lett.* **88**, 228304 (2002).
- [24] E. Paladino, Y. M. Galperin, G. Falci, and B. L. Altshuler, *Rev. Mod. Phys.* **86**, 361 (2014).
- [25] O. Astafiev, Yu. A. Pashkin, Y. Nakamura, T. Yamamoto, and J. S. Tsai, *Phys. Rev. Lett.* **93**, 267007 (2004)
- [26] John M. Martinis, K. B. Cooper, R. McDermott, Matthias Steffen, Markus Ansmann, K. D. Osborn, K. Cicak, Seongshik Oh, D. P. Pappas, R. W. Simmonds, and Clare C. Yu, *Phys. Rev. Lett.* **95**, 210503 (2005).
- [27] S. W. Jung, T. Fujisawa, Y. Hirayama and Y. H. Jeong, *Appl. Phys. Lett.* **85**, 768 (2004).
- [28] O. E. Dial, M. D. Shulman, S. P. Harvey, H. Bluhm, V. Umansky, and A. Yacoby, *Phys. Rev. Lett.* **110**, 146804 (2013).
- [29] F. Beaudoin and W. A. Coish, *Phys. Rev. B* **91**, 165432 (2015).
- [30] Jun Yoneda, Kenta Takeda, Tomohiro Otsuka, Takashi Nakajima, Matthieu R. Delbecq, Giles Allison, Takumu Honda, Tet-suo Kodera, Shunri Oda, Yusuke Hoshi, Noritaka Usami, Kohei M. Itoh and Seigo Tarucha, *Nature Nanotech.* **13**, 102 (2018).
- [31] Elliot J. Connors, JJ Nelson, Haifeng Qiao, Lisa F. Edge, and John M. Nichol, arXiv:1907.07549 (unpublished).
- [32] Filip K. Malinowski, Frederico Martins, Łukasz Cywiński, Mark S. Rudner, Peter D. Nissen, Saeed Fallahi, Geoffrey C. Gardner, Michael J. Manfra Charles M. Marcus, and Ferdinand Kuemmeth, *Phys. Rev. Lett.* **118**, 177702 (2017).
- [33] Pascal Cerfontaine, René Otten, M. A. Wolfe, Patrick Bethke, and Hendrik Bluhm, arXiv:19001.00851 (unpublished).
- [34] J. Bergli, Y. M. Galperin, and B. L. Altshuler, *New J. Phys.* **11**, 025002 (2009).
- [35] Guy Ramon, *Phys. Rev. B* **92**, 155422 (2015).
- [36] Łukasz Cywiński, *Phys. Rev. A* **90**, 042307 (2014).
- [37] Shlomi Kotler, Nitzan Akerman, Yinnon Glickman, and Roe Ozeri, *Phys. Rev. Lett.* **110**, 110503 (2013).
- [38] Ryogo Kubo, *J. Phys. Soc. Jpn.* **17**, 1100 (1962).
- [39] S. Kogan, *Electronic Noise and Fluctuations in Solids*, Cambridge University Press (1996).
- [40] Y. M. Galperin, B. L. Altshuler, and D. V. Shantsev, in *Funda-*

- mental Problems in Mesoscopic Physics*, edited by I. V. Lerner, B. L. Altshuler, and Y. Gefen (Kluwer, Dordrecht, 2004), pp. 141-165.
- [41] Our definition of the noise cumulants in Eq. (2) excludes the coupling strength, v , and the resulting noise correlators and polyspectra should be multiplied by v^k for correct evaluation of their weight in the cumulant expansion. Here, k ($k - 1$) corresponds to the k -point correlator ($k - 1$ polyspectrum).
- [42] See Supplemental Material at <http://link.aps.org/Supplemental/>
- [43] V. Chandran and S. A. Elgar, IEEE Trans. Signal Proc. **42**, 229 (1994).
- [44] Piotr Szańkowski and Łukasz Cywiński, Phys. Rev. A **97**, 032101 (2018).
- [45] Ashok Ajoy, Gonzalo A. Álvarez, and Dieter Suter, Phys. Rev. A **83**, 032303 (2011).
- [46] We expect that a simple preliminary measurement protocol can be carried out to calibrate the measurement time T with the average switching rate of the RTN at hand.
- [47] Guy Ramon, Phys. Rev. B **86**, 125317 (2012).
- [48] Our analysis does not include pulse errors, but for most scenarios it is expected that pulse errors will become more dominant as the number of pulses increases. From this perspective, it is desirable to keep M as low as possible, while maintaining a reasonably accurate delta-approximation.
- [49] Benjamin Abel and Florian Marquardt, Phys. Rev. B **78**, 201302(R) (2008).
- [50] H. J. Wold, H. Brox, Y. M. Galperin, and J. Bergli, Phys. Rev. B **86**, 205404 (2012).
- [51] C. Müller, J. Lisenfeld, A. Shnirman and S. Poletto, Phys. Rev. B **92**, 035442 (2015).
- [52] Dapeng Ding, David van Driel, Lino M. C. Pereira, Jared F. Bauters, Martijn J. R. Heck, Gesa Welker, Michiel J. A. de Dood, André Vantomme, John E. Bowers, Wolfgang Löffler, and Dirk Bouwmeester, arXiv:1811.05248 (unpublished).

Supplemental Material for "Trispectrum reconstruction of non-Gaussian noise"

Guy Ramon*

Department of Physics, Santa Clara University, Santa Clara, CA 95053

I. RTN TRISPECTRUM

The calculation of the RTN trispectrum in Eq. (7) of the main text involves piecewise evaluation of time integrals over the three time separations, $\tau_j = t_{j+1} - t_1$, in the four-point noise correlators. For $t_1 \leq t_2 \leq t_3 \leq t_4$ the four-point correlator reads: $\langle \xi(t_1)\xi(t_2)\xi(t_3)\xi(t_4) \rangle = e^{-2\gamma(\tau_3 - \tau_2 + \tau_1)}$ and other time orderings result in corresponding interchanges in the exponential. One can then group piecewise integrals corresponding to the six possible τ_j -orderings. A further simplification of the integrands yields:

$$S_3(\vec{\omega}_3) = -8 \int_0^\infty \left\{ \int_{\tau_3}^\infty \int_{\tau_3}^\infty e^{-2\gamma(\tau_1 + \tau_2)} \mathcal{F}_3 d\tau_1 d\tau_2 + \int_0^{\tau_3} \int_{\tau_2}^\infty e^{-2\gamma(\tau_1 + \tau_3)} \mathcal{F}_2 d\tau_1 d\tau_2 + \int_{\tau_3}^\infty \int_0^{\tau_3} e^{-2\gamma(\tau_2 + \tau_3)} \mathcal{F}_1 d\tau_1 d\tau_2 + \int_0^{\tau_3} \int_0^{\tau_2} e^{-2\gamma(\tau_2 + \tau_3)} \mathcal{F}_1 d\tau_1 d\tau_2 \right\} d\tau_3, \quad (1)$$

where we defined

$$\mathcal{F}_i \equiv \cos \omega_1 \tau_1 \cos(\omega_2 \tau_2 + \omega_3 \tau_3) \cosh 2\gamma \tau_i - \sin \omega_1 \tau_1 \sin(\omega_2 \tau_2 + \omega_3 \tau_3) \sinh 2\gamma \tau_i + \cos \omega_1 \tau_1 \cos(\omega_2 \tau_2 - \omega_3 \tau_3) e^{-2\gamma \tau_i}. \quad (2)$$

Performing the integrals in Eq. (1) results in the RTN trispectrum formula given by Eq. (7) in the main text.

II. TRISPECTRUM PRINCIPAL DOMAIN

As manifested by Eq. (7) in the main text, the trispectrum is invariant under the following operations: (i) 6 permutations, (ii) 2 complex conjugations, $S_3(\omega_1, \omega_2, \omega_3) = S_3(-\omega_1, -\omega_2, -\omega_3)$, and (iii) stationarity, $\omega_i \rightarrow -\Sigma \vec{\omega}_3, \forall i$. These symmetries define 48 regions in the three-dimensional frequency space with identical $S_3(\vec{\omega}_3)$ values. The principal domain is found as: $\text{PD} = \{0 \leq \omega_1, 0 \leq \omega_2 \leq \omega_1, -\omega_2 \leq \omega_3 \leq \omega_2\}$. Discretizing the space with integer multiples of the fundamental frequency, $2\pi/T$, and retaining n_3^{max} harmonics, we find the number of points in the truncated principal domain, \mathcal{D}_3 , to be

$$n_{\text{TRI}} = \frac{1}{6} (n_3^{\text{max}} + 1) (n_3^{\text{max}} + 2) (2n_3^{\text{max}} + 3). \quad (3)$$

Table I lists the trispectrum principal domain region boundaries, and their respective multiplicities, $\Omega_3(\vec{n}_3)$, as well as the number of frequency points in each region (adding up to n_{TRI}). Notice that $\frac{1}{2}(1 + n_3^{\text{max}})(2 + n_3^{\text{max}})$ points of the total of n_{TRI} points include a zero frequency, thereby requiring at least one control sequence with zero filtering order for reconstruction. For $n_3^{\text{max}} = 8$, used in our reconstructions, $n_{\text{TRI}} = 285$, of which 45 points include at least one zero frequency.

TABLE I. Properties of the discretized and truncated principal domain of the trispectrum

Region	Boundary	Ω_3	Number of points
Inside		48	$\frac{1}{6} n_3^{\text{max}} (n_3^{\text{max}} - 1) (2n_3^{\text{max}} - 1)$
Faces	$\omega_2 = \omega_1 \neq 0$	24	$(n_3^{\text{max}})^2$
	$\omega_3 = \omega_2 \neq 0$	24	$\frac{1}{2} n_3^{\text{max}} (n_3^{\text{max}} - 1)$
	$\omega_3 = -\omega_2 \neq 0$	24	$\frac{1}{2} n_3^{\text{max}} (n_3^{\text{max}} - 1)$
Edges	$\omega_2 = \omega_3 = 0, \omega_1 \neq 0$	12	n_3^{max}
	$\omega_1 = \omega_2 = \omega_3 \neq 0$	8	n_3^{max}
	$\omega_1 = \omega_2 = -\omega_3 \neq 0$	6	n_3^{max}
Vertices	$\omega_1 = \omega_2 = \omega_3 = 0$	1	1

* gramon@scu.edu

III. CONTROL SEQUENCE SELECTION FOR FAITHFUL NON-GAUSSIAN NOISE RECONSTRUCTION

The main challenge in implementing the perturbative approach of Norris *et al.* [1] is that even with only the first several cumulants retained and modest grids of frequency points employed, the multidimensional polyspectra require a large number of spectrally distinct control sequences. This creates an inherent tradeoff between the need to accurately capture the cumulants using a finite set of points and the tendency of sequences that meet these error thresholds to possess similar filtering properties, thereby resulting in ill-conditioned reconstruction matrices. A careful sequence selection is thus crucial for any practical implementation.

We have developed an algorithm for generation and selection of pulse sequences that enables a faithful reconstruction of the PSD and trispectrum of a single RTN over a wide range of parameters. We first generate a large number of distinct sequences satisfying a set of criteria detailed below and calculate their exact and approximate noise cumulants for a nominal RTN source (subsequent adjustments of these cumulants for different TLF parameters pose minimal computational overhead). Next we choose a subset of these sequences, by employing a two-step optimization of the reconstruction matrix. This layered process enables us to quickly retrieve information needed for an optimized and efficient sequence selection. In the following we provide details of the criteria employed in the selection process.

A. Sequence Pool Generation

All the generated base sequences have a fixed time, $T = 256\delta$, where δ is the minimum time resolution. We scale times with inverse RTN switching rate, γ , taken to be 1, such that $\delta = 1/(16\gamma)$. Mixed-order CDD (MCDD) sequences are generated, where each segment is characterized by time T_i , such that $\sum_i T_i = T$, CDD order, l_i , and its respective number of pulses n_p^i given by

$$n_p^i = \frac{1}{3} [2^{l_i+1} - 2 + (l_i \bmod 2)]. \quad (4)$$

As discussed in the main text, FID segments ($n_i = 0$) are allowed and needed for reconstruction of zero-frequency points. All MCDD sequences obey the following criteria:

- i. $T_i/\delta \bmod 2^{l_i} = 0$, ensuring pulse times are at integer multiples of δ .
- ii. Minimum interpulse separation is set at $\tau = 4\delta$. This condition limits the maximum CDD order to 6, but the only sequence in compliance (single segment with $T_1 = T$ and $n_p^1 = 42$) induces a large truncation error, thus our effective limit is at CDD order of 5.
- iii. The total number of pulses is even to avoid nonzero contributions from odd multiples of π/T that will double the number of frequency points necessary for faithful reconstruction.
- iv. sequences are repeated $M = 30$ times, unless otherwise noted. The effects of base sequence repetition on the reconstruction quality and robustness against measurement errors are presented in the main text in Fig. 3 and following discussion, and in section IV below.

We include non-symmetric sequences in the pool to increase the number of distinct sequences, i.e., non-balanced sequences are permitted. We have also generated pools of mixed-CPMG sequences and found them to provide similar reconstruction results, as compared with MCDD sequences. Large (over a million) pools of distinct sequences satisfying the above conditions are generated, and their resulting delta approximated second and fourth noise cumulants for a nominal RTN source with $\gamma = 1$ are calculated, using Eqs. (8) and (9) in the main text, and taking $n^{\max} = 32$, and $n_3^{\max} = 8$. Exact calculation of the cumulants for the repeated sequences is carried out in time domain, using recursive formulae detailed in Sec. V below. All sequence information (segment lengths, CDD orders, pulse times, and exact and approximate C_2 and C_4 calculations) is recorded for quick retrieval, allowing us to select an optimized set of sequences for a given reconstruction task.

B. Sequence Selection for the Reconstruction Matrix

PSD and trispectrum reconstructions at $n_{\text{PSD}} = 33$ and $n_{\text{TRI}} = 285$ frequency points in the truncated principal domains require $n_{\text{seq}} = 318$ control sequences. The elements of the reconstruction matrix in Eq. (10) in the main text read

$$A_{ik} = \begin{cases} \frac{Mv^2}{2T} \Omega_1(n_k) \left| \tilde{f}_T^i \left(\frac{2\pi}{T} n_k \right) \right|^2, & 1 \leq k \leq n_{\text{PSD}} \\ -\frac{Mv^4}{24T^3} \Omega_3(\vec{n}_3^k) \prod_{j=1}^3 \tilde{f}_T^i \left(\frac{2\pi}{T} \vec{n}_3^k(j) \right) \tilde{f}_T^i \left(-\frac{2\pi}{T} \Sigma \vec{n}_3^k \right), & n_{\text{PSD}} + 1 \leq k \leq n_{\text{seq}} \end{cases} \quad (5)$$

where i denotes the sequence index and k enumerates the frequency points in either \mathcal{D}_1 or \mathcal{D}_3 .

Truncating cumulants higher than C_4 seems to suggest that it should be easier to reconstruct noise from weakly coupled RTNs. While the PSD is largely unaffected by the minute non-Gaussian contributions, and is therefore easily recovered, trispectrum reconstruction in this regime is challenging. Since the second cumulant elements of the reconstruction matrix are much larger than the fourth cumulant elements, small errors in the former introduce large deviations from the correct trispectrum. For $\eta = v/\gamma = 0.1$, one needs to place a C_2 error threshold that is two orders of magnitude lower than that for C_4 . As a result, only a small subset of the sequences in the pool can be used for adequate trispectrum reconstruction.

Our sequence selection algorithm proceeds in two steps. First we retain a subset of pool sequences that pass both absolute and relative cumulants error thresholds, defined as follows. Setting

$$\begin{aligned}\Delta C_2^i &= |C_{2,\text{app}}^i - C_{2,\text{ex}}^i| \\ \Delta C_4^i &= |C_{4,\text{app}}^i - C_{4,\text{ex}}^i|,\end{aligned}\quad (6)$$

as the cumulant errors of the truncated δ -approximation for sequence i , we define the second cumulant absolute error as $\Delta C_2^i/C_{2,\text{ex}}^i$, and similarly the fourth cumulant absolute error, and require these errors to fall below threshold values \mathcal{E}_2 and \mathcal{E}_4 , respectively. Sequences that pass the relative cumulant error test satisfy

$$\frac{\Delta C_2^i}{\min(|C_{2,\text{ex}}^j|, \frac{v^2}{12}|C_{4,\text{ex}}^j|)} \bigcap \frac{\frac{v^2}{12}\Delta C_4^i}{\min(|C_{2,\text{ex}}^j|, \frac{v^2}{12}|C_{4,\text{ex}}^j|)} < \mathcal{E}_{\text{set}}, \quad \forall i, \quad (7)$$

where j runs over all sequences in the subset. The three error thresholds, \mathcal{E}_2 , \mathcal{E}_4 , and \mathcal{E}_{set} , are gauged to generate a subset of size $\sim 2n_{\text{seq}}$ (600-700 sequences for the examples shown in this paper), which in our experience is sufficient to ensure a reasonably well-conditioned final set of n_{seq} sequences, generated in the second step (see below). As a concrete example, for the weak coupling case, $v = 0.1$, our optimized set for $M = 30$ is formed with error thresholds of $\mathcal{E}_2 = 5 \times 10^{-6}$, $\mathcal{E}_4 = 5 \times 10^{-3}$, and $\mathcal{E}_{\text{set}} = 0.0054$. At stronger couplings the stringent threshold for \mathcal{E}_2 is relaxed considerably, thus, while one can potentially optimize sequence sets for a given coupling strength when this information is a-priori known, sequence sets optimized for weak coupling serve, in practice, as good basis for noise reconstruction up to intermediate coupling strengths. A more sophisticated algorithm can adjust the three error thresholds adaptively through feedback given by the reconstruction quality. At yet higher coupling strengths, $\eta \gtrsim 0.8$, errors due to the cumulant series truncation dominate. One way to extend the applicability of the DDNS protocol to the strong coupling regime is to include a parameterized correction term, optimized through the measured qubit signals afflicted by the (unknown) RTN source. These corrected reconstructions are depicted by blue squares in all relevant figures in the main text and in the supplemental material. While a full analysis of error-correcting noise reconstruction protocols solely based on qubit signal measurements is underway, our preliminary work suggests that these protocols are feasible with reasonable measurement overhead.

The final step in the sequence selection process is to find a subset of n_{seq} sequences that minimizes the condition number of the reconstruction matrix, A , defined in Eq. (10) in the main text. As mentioned above, sequences that pass the stringent error threshold screening at weak coupling tend to have similar filtering, resulting in large condition numbers. The problem of extracting a well conditioned subset from a larger rectangular matrix has been studied extensively, given its many applications spanning from rank revealing factorization to functional and harmonic analysis. While finding a subset with the absolute minimal condition number is believed to be NP-hard, many efficient algorithms that guarantee bounds on the singular values of a given subset have been developed for various cases [2–4]. For the problem at hand, we have adapted an efficient algorithm for maximal orthogonalization by Knuth [5] that provides orders-of-magnitude reduction in the condition number of A , as compared with random subset selection. While ill-conditioned reconstruction matrices must be avoided to ensure numerical stability, our algorithm is designed with efficiency in mind to guarantee that we are working with sequence sets for which reconstruction errors due to large condition numbers are always negligible, as compared with errors due to cumulant series truncation and cumulant approximation.

Our sequence selection process is demonstrated in Fig. 1, where we present PSD and trispectrum reconstructions for coupling strengths of $v = 0.1$ and $v = 0.8$. The top panel row depicts reconstruction results with ‘randomly’ selected sequences out of a large pool of MCDD base-sequences (we still verify that all selected sequences are distinct). Trispectrum reconstructions (panels (b) and (j)) is very poor, particularly in the weak-coupling case, since second cumulant errors can be orders of magnitude larger than the fourth cumulant actual values. The second row of panels shows reconstructions with sequences randomly selected from a subset passing absolute cumulant error thresholds, whereas the third row shows results with sequences passing both absolute and relative cumulant error thresholds. The bottom row shows our final results, as presented in the main text, using a sequence set that minimizes the reconstruction matrix condition number. We note that the residual error due to large condition numbers is substantially larger in the weak-coupling case, where sequences that meet the needed error thresholds tend to have similar filtering properties (compare deviations between red circles in panels (f) and (h) to those between panels (n) and (p), and note that in the latter case, deviation of the reconstructed trispectrum from the theoretical curve is predominantly due to cumulant series truncation, as evidenced by the corrected results depicted by blue squares in panel (p)).

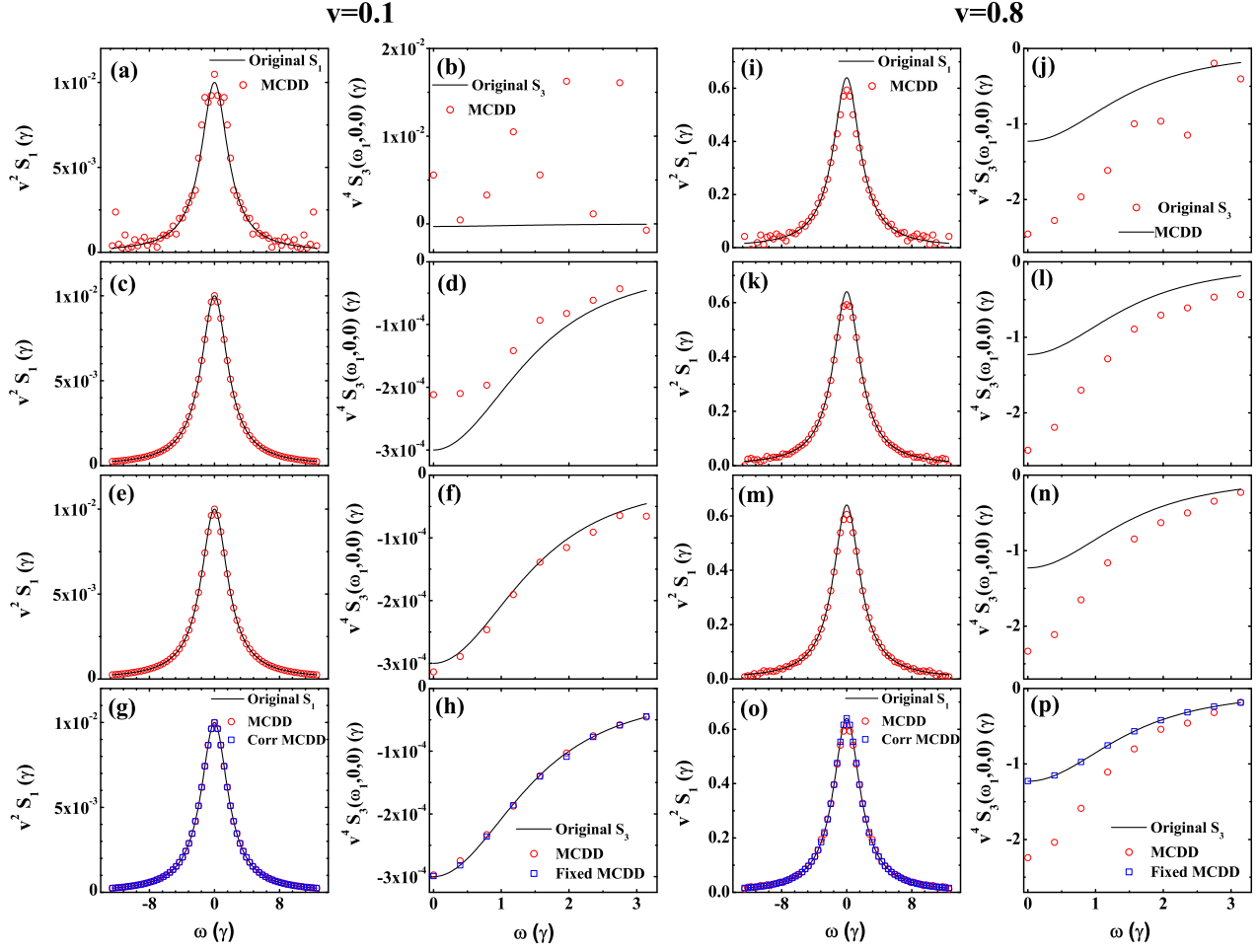


FIG. 1. (Color online) Sequence selection evolution for RTN reconstruction with coupling strengths $v = 0.1$ (panels a-h) and $v = 0.8$ (panels i-p). Panels (a), (b), (i), and (j) show results generated from ‘randomly’ selected distinct sequences of a pool of size $\sim 400,000$. In panels (c), (d), (k), and (l) sequences are selected from a subset of 23,386 sequences passing the absolute cumulant error thresholds $\mathcal{E}_2 = 5 \times 10^{-6}$, $\mathcal{E}_4 = 5 \times 10^{-3}$. Panels (e), (f), (m), and (n) depict reconstructions using sequences that pass the above absolute error thresholds *and* the relative error test, Eq. (7), with $\mathcal{E}_{\text{set}} = 0.0054$ (633 sequences). Finally, panels (g), (h), (o), and (p) show reconstructions using a sequence set optimized to minimize the condition number of the reconstruction matrix, A . These sets are used to generate the results presented in the main text. In all panels solid lines depict the theoretical PSD and trispectrum cut along $\omega_2 = \omega_3 = 0$, normalized with v^2 and v^4 , respectively, and measured in units of the RTN average switching rate, γ . Red circles depict reconstruction results and blues squares (in the final step only) show corrected reconstruction results. Base sequences are repeated 30 times.

In Fig. 2 we compare trispectra reconstructions using a single sequence set, optimized for weak coupling, $v = 0.1$ (red circles) to those generated with sequence sets optimized for each coupling strength (black crosses). These results demonstrate our ability to successfully reconstruct trispectra of RTNs with arbitrary coupling strengths using a generic sequence protocol, paving the way to experimental characterization of a-priori unknown RTN sources. Using the reconstruction quality definition given by Eq. (11) in the main text, we find that \mathcal{Q} deteriorates by an order of magnitude, from values in the range of $1.8 \times 10^{-3} - 2.8 \times 10^{-3}$ with protocols optimized per each coupling strength to $\mathcal{Q} = 0.02$ with a single sequence protocol optimized for weak coupling. Reconstruction quality remains nevertheless satisfactory.

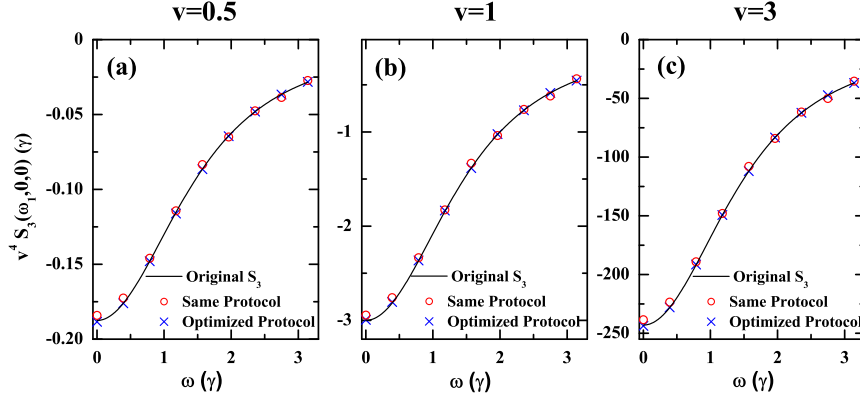


FIG. 2. (Color online) Trispectrum reconstruction of RTN with coupling strength of: (a) $v = 0.5$, (b) $v = 1$, and (c) $v = 3$. Solid lines depict the theoretical trispectrum cut along $\omega_2 = \omega_3 = 0$. Red circles depict reconstructions with a single sequence set, selected at weak-coupling ($v = 0.1$), whereas black crosses correspond to reconstruction with sequence sets optimized to each coupling strength scenario. Base sequences are repeated $M = 30$ times. Results in all plots include cumulant series truncation correction.

IV. RECONSTRUCTION ROBUSTNESS

We tested the effectiveness of our reconstruction protocols in the presence of measurement errors, simulated by replacing the theoretical (exact) values for the qubit signal decay, $W(T)$, with a 'measured' value, $(1 + \alpha\zeta_j)W(T)$, where α is the noise amplitude and ζ_j is a number randomly drawn from a uniform distribution on the interval $(-1, 1)$, corresponding to the j th measurement. The 'measured' attenuation factor reads

$$\chi_j^{\text{meas}}(T) = \chi(T) - \ln(1 + \alpha\zeta_j), \quad (8)$$

and we perform RTN reconstruction simulations by averaging over 20,000 realizations of the measurement noise.

Fig. 3 shows PSD and trispectra reconstruction results for three coupling strengths with several measurement noise amplitudes. As expected, trispectrum reconstruction at weak coupling, depicted in panel (d) is particularly challenging and requires very low levels of measurement noise. As coupling strength is increased, reconstruction deviations due to measurement noise are more equally distributed between the PSD and trispectrum, and higher levels of measurement noise become tolerable.

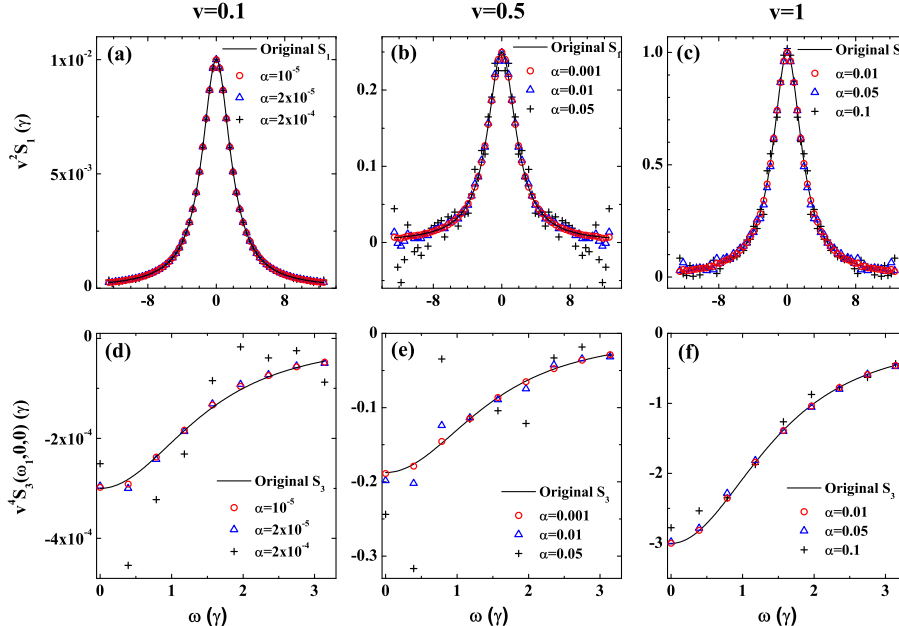


FIG. 3. (Color online) PSD (panels (a)-(c)) and trispectrum (panels (d)-(f)) reconstruction for three coupling strengths and three measurement noise levels. All results are obtained with the same sequence protocol, optimized for $v = 0.1$ and $M = 30$ and include cumulant series truncation correction. As coupling strength increases, faithful reconstruction is maintained for larger measurement errors.

Lastly, we studied the effects of base sequence repetition, M , on the quality of trispectrum reconstruction. Fig. 4 shows trispectrum reconstruction quality, \mathcal{Q} , defined in Eq. (11) in the main text vs. number of repetitions for several coupling strengths with a single set optimized for $v = 0.1$ and $M = 30$ (blue crosses) and with sets optimized for each v and M value (red circles). We note that increased repetition does not guarantee better reconstruction, as one might expect, in particular when using a single non-optimized sequence set. The reason that a protocol optimized for a given M will under-perform at higher M is because there exists an interplay between the filter function peak area (determined by M) and errors induced by truncated frequencies—the latter often being compensated by the wider filter function peaks that result in implementing fewer repetitions. As discussed above, trispectrum reconstruction at weak coupling is challenging and requires the control protocol to be tailored to the task. This is manifested in Figure 4(a) where any slight deviation from the predefined value of $M = 30$ results in orders of magnitude deterioration in \mathcal{Q} . At stronger coupling strengths, where non-Gaussian behavior is more pronounced, and is thus more easily detected, adequate reconstruction can be maintained over wider range of M values.

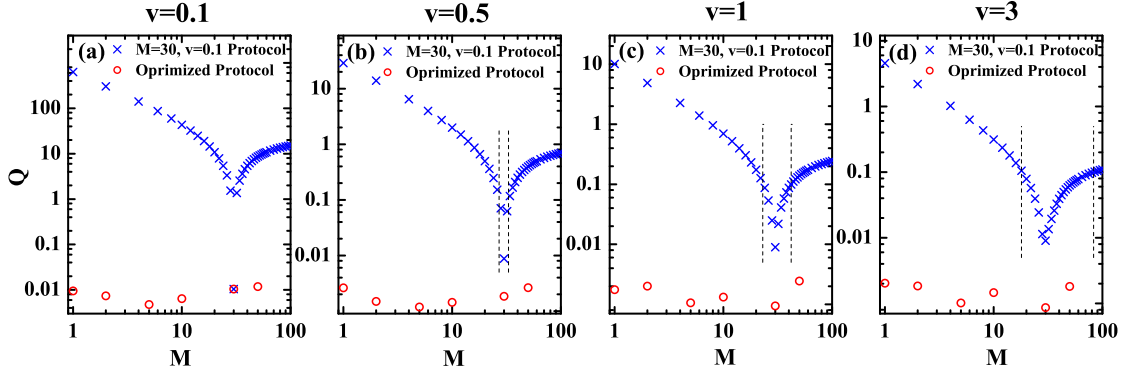


FIG. 4. (Color online) Trispectrum reconstruction quality vs. number of base sequence repetitions for several coupling strengths. Blue crosses correspond to results with a generic control protocol, optimized for $v = 0.1$ and $M = 30$, whereas red circles depict results obtained with sequence sets optimized for each v and M value. Vertical dashed lines mark the range of M values for which \mathcal{Q} falls below 10% (no such range exists for $v = 0.1$).

V. SECOND AND FOURTH CUMULANTS FOR RTN UNDER MIXED-CDD PULSE SEQUENCES

For any sequence of n_p control pulses at times $\{\tau_k\}$, with $\tau_0 = 0$, $\tau_{n_p+1} = T$, we can perform the time integrals piecewise, resulting in recursive sum forms that are suitable for an efficient numerical evaluation. The second and fourth cumulants are found from the noise moments, $M_k(T)$

$$C_2(T) = M_2(T) = \int_0^T dt_1 e^{-2\gamma t_1} f_T(t_1) \int_0^{t_1} dt_2 e^{2\gamma t_2} f_T(t_2) = \frac{1}{2\gamma^2} \left[B(n_p) + (-1)^{n_p} e^{-2\gamma(T-\tau_{n_p})} A(n_p) + 2\gamma T \right], \quad (9)$$

and

$$C_4(T) = M_4(T) - 3[M_2(T)]^2, \quad (10)$$

with

$$\begin{aligned} M_4(T) &= \int_0^T dt_1 e^{-2\gamma t_1} f_T(t_1) \int_0^{t_1} dt_2 e^{2\gamma t_2} f_T(t_2) \int_0^{t_2} dt_3 e^{-2\gamma t_3} f_T(t_3) \int_0^{t_3} dt_4 e^{2\gamma t_4} f_T(t_4) \\ &= \frac{4!}{(2\gamma)^4} \left\{ \sum_{n_1=0}^{n_p} \left[(-1)^{n_1+1} C(n_1) \left(e^{-2\gamma(\tau_{n_1+1}-\tau_{n_1})} - 1 \right) + (B(n_1) - 1) 2\gamma(\tau_{n_1+1} - \tau_{n_1}) \right. \right. \\ &\quad \left. \left. - (-1)^{n_1} A(n_1) \left(e^{-2\gamma(\tau_{n_1+1}-\tau_{n_1})} (1 + 2\gamma\tau_{n_1+1}) - (1 + 2\gamma\tau_{n_1}) \right) \right] + 2(\gamma T)^2 \right\}. \end{aligned} \quad (11)$$

In Eqs. (9) and (11) we defined

$$\begin{aligned}
A(n) &= 2 \sum_{n_1=0}^n (-1)^{n_1} e^{-2\gamma(\tau_n - \tau_{n_1})} - e^{-2\gamma\tau_n}, \\
B(n) &= \sum_{n_1=0}^{n-1} (-1)^{n_1} \left(e^{-2\gamma(\tau_{n_1+1} - \tau_{n_1})} - 1 \right) A(n_1) - (-1)^n A(n), \\
C(n) &= \sum_{n_1=0}^{n-1} \left\{ e^{-2\gamma\tau_n} \left[(-1)^{n_1} (B(n_1) - 1) (e^{2\gamma\tau_{n_1+1}} - e^{-2\gamma\tau_{n_1}}) + (-1)^{n_1} 2\gamma (\tau_{n_1+1} e^{2\gamma\tau_{n_1+1}} - \tau_{n_1} e^{2\gamma\tau_{n_1}}) \right] \right. \\
&\quad \left. + 2\gamma A(n_1) e^{-2\gamma\tau_{n_1}} (\tau_{n_1+1} - \tau_{n_1}) \right\} - (-1)^n B(n) - 2\gamma A(n) \tau_n - (-1)^n (2\gamma\tau_n - 1). \tag{12}
\end{aligned}$$

Implementation of sequence repetition follows straightforwardly by concatenating the base sequence M times, effectively extending the sequence time to MT . We have also derived a formula for the RTN second cumulant of a repeated sequence in terms of that of the base sequence. For the employed sequences with even number of pulses we find

$$C_2(MT) = MC_2(T) + [C_2(T) + C_2^{\gamma \rightarrow -\gamma}(T)] \frac{e^{-2\gamma T(M-1)} - M + (M-1)e^{2\gamma T}}{(1 - e^{2\gamma T})^2}. \tag{13}$$

While all the reconstruction results presented in the main text are generated with mixed-CDD (MCDD) sequences, we have also considered two- and three-segment CPMG base-sequences. For these mixed-CPMG sequences, closed-form formulae of both the second and fourth cumulants can be obtained for repeated base-sequences, using the results of ref. [6] as a starting point.

-
- [1] Leigh M. Norris, Gerardo A. Paz-Silva, and Lorenza Viola, Phys. Rev. Lett. **116**, 150503 (2016).
 - [2] J. Bourgain and L. Tzafriri, Israel J. Math, **57** 137 (1987).
 - [3] J. A. Tropp, Proc. 2009 ACM-SIAM Symp. Discrete Algorithms (SODA), 978 (2009).
 - [4] Stéphane Chrétien and Sébastien Darses, arXiv:1509.00748v2 [math.FA] (unpublished).
 - [5] Donald E. Knuth, Linear and Multilinear Algebra **17**, 1 (1985).
 - [6] Guy Ramon, Phys. Rev. B **92**, 155422 (2015).